Title:

Nernstian stability of the Eh–O_2 relationship reveals redox structural shifts

Authors and Affiliations:

Kyoko Morimoto[1], Mana Ito[2], Katsutoshi Ito[2], and Mayumi Seto[3*]

[1] Department of Chemistry, Biology, and Environmental Sciences, Nara Women's University, Kita-Uoya Nishimachi, Nara 630-8506, Japan

[2] Environmental Conservation Division, Environment and Fisheries Applied Research Department, Fisheries Technology Institute, Japan Fisheries Research and Education Agency, 2-17-5 Maruishi, Hatsukaichi, Hiroshima 739-0452, Japan

[3] Department of Environmental and Natural Resource Sciences, Faculty of Agriculture, Tokyo University of Agriculture and Technology, 3-5-8, Saiwaicho, Fushu-shi, Tokyo, 630-8506, Japan

Preprint Statement:

This manuscript is a non-peer-reviewed preprint submitted to *EarthArXiv*. The manuscript has been simultaneously submitted for peer review to *Limnology and Oceanography*.

Corresponding author: Mayumi Seto

Email: seto@go.tuat.ac.jp

Abstract

Oxidation-reduction potential (Eh) offers a compact descriptor of aquatic redox status, yet its interpretation is obscured by the many co-occurring electron-transfer reactions that determine it. We tested the hypothesis that the persistence of a linear, Nernstian relationship between Eh and ln[O_2] reflects the robustness of the underlying redox structure. Using 18 months of depth profiles and high-frequency measurements in a disturbance-prone pond, we found that Eh increased linearly with ln[O_2] across depths and seasons (slope = 0.079 V; R^2 = 0.38), indicating a persistent Nernstian slope. A sediment-inflow event temporarily collapsed this slope at one site, revealing a reorganization of the local redox network. High-frequency observations further showed that rainfall-driven oxygen spikes scarcely affected sediment Eh, demonstrating that short-term hydrological disturbances do not alter the prevailing redox structure. Additionally, causal analysis (EchoNet) showed that Eh was driven primarily by temperature rather than dissolved oxygen, indicating that oxygen's influence is dispersed across many intertwined reaction pathways. Together, these results show that, although the Eh–O_2 relationship cannot resolve detailed reaction pathways, co-located and continuous Eh–O_2 monitoring provides a robust indicator of redox structural stability and a practical tool for detecting structural redox shifts in shallow aquatic systems.

Keywords

Redox potential, Dissolved oxygen, Redox network structure, High-resolution monitoring, Causal time-series analysis

1. Introduction

Redox processes regulate the transformations of carbon, nitrogen, sulfur, iron, and other redox-sensitive elements, thereby shaping nutrient cycling, organic-matter degradation, and contaminant mobility in aquatic environments (Borch et al. 2010; Violante et al. 2010; Tandon and Singh 2016; Lau et al. 2018). Because these processes are governed by electron transfers among multiple redox couples, the oxidation-reduction potential (Eh) has long been viewed as a convenient integrator of overall redox status.

Despite this conceptual appeal, Eh remains far less widely used than pH in routine monitoring of surface waters. Two issues in particular limit its interpretability. First, although Eh is often treated as a diagnostic indicator of which redox reactions are occurring and to what extent, in practical it cannot serve this function. A measured Eh value represents a mixed potential arising from multiple, simultaneously operating electron-transfer reactions, rather than the equilibrium potential of any individual couple (Stumm and Morgan 1996; Stefánsson et al. 2005). Consequently, measured Eh commonly deviates by hundreds of millivolts from the potentials calculated for specific couples such as O_2/H_2O, NO^{3-}/NO^{2-}, Fe^{2+}/Fe^{3+} (Lindberg and Runnells 1984; Teasdale et al. 1998; Ramesh Kumar and Riyazuddin 2012). Second, redox conditions in shallow waters are highly dynamic: solute fluxes and hydrological or mixing events continually reshape the distribution of oxidants and reductants. These rapid fluctuations mean that the Eh measured at a given moment may not represent a stable or spatially coherent redox state. Together, these factors imply that single-time measurements of Eh cannot be directly interpreted as indicators of how redox processes are progressing in the field.

In most oxygenated surface waters, molecular oxygen is the predominant terminal electron acceptor. Organic matter, typically the abundant electron donor in such systems,

supplies electrons to O_2 through a network of direct and indirect pathways that may involve nitrogen, iron or sulfur intermediates (Fig. 1a). In principle, the sensitivity of Eh to changing O_2 concentrations should contain information about the organization of this upstream reaction network. If we denote by n_{eff} the effective number of electrons ultimately transferred to O_2 per mole of reaction flux through this upstream network, then the response of Eh to dissolved oxygen can be expressed as follows:

$$\mathrm{Eh} = \mathrm{Eh}^{*} + \frac{RT}{n_{eff}F} \ln\{\mathrm{O_2}\}, \quad (1)$$

This formulation does not imply equilibrium with the O_2/H_2O couple. Rather, it states that a stable linear $\ln\{O_2\}$–Eh relationship requires the upstream redox network to maintain a consistent electron-supply stoichiometry to O_2, even as environmental conditions change. Conversely, departures from this relationship should indicate structural reorganization of the underlying redox system, whether driven by changes in organic-matter supply, metal loads, sediment inputs, or microbial activity.

Despite this theoretical foundation, the empirical stability, disturbance sensitivity, and diagnostic value of the $\ln\{O_2\}$–Eh slope have rarely been assessed in natural or managed surface waters. It remains unclear whether this relationship persists across depths and seasons, whether disturbances produce detectable deviations, and whether O_2 dynamics dominate short-term Eh variability.

Here we address these gaps using a disturbance-prone artificial pond as a natural stress-test system. We combined 18 months of depth-resolved profiles with high-frequency measurements to examine (1) whether the $\ln\{O_2\}$–Eh relationship maintains a stable Nernstian slope, (2) whether slope deviations correspond to redox reorganization

during disturbances, and (3) whether time-series analysis identifies O_2 as a primary driver of Eh variability. Our aim is to evaluate whether the Eh–O_2 relationship can serve as a simple, system-level indicator of structural redox stability in shallow aquatic environments.

2. Material and Methods

2.1 Monitoring site

A small artificial pond (≈ 10 m^3; 34°41’14.5”N, 135°49’45.9”E) in Nara Prefecture, Japan, served as the study site (Fig. 1b). The pond is surrounded by trees and receives substantial inputs of leaf litter in autumn. The bottom substrate consists primarily of gravel mixed with decomposed leaves, and no aquatic macrophytes are present. Water depth varies spatially, with Site A exceeding 40 cm, Site B between 20−40 cm, and Site C less than 20 cm.

The pond is enclosed on three sides by a waterproof mortar structure that prevents lateral inflow or outflow. Before August 2022, a peripheral water channel had not yet been constructed (Fig. 1c). After its construction, water was pumped intermittently (daytime only) from Site D using a solar-powered system. Pumping volumes measured during August 26−September 14, 2022, averaged 499 L day^{-1} (range 124−1300 L day^{-1}).

Monitoring was conducted at six sites (A0, A1, B, C, D, and E). Sites A0 and A1 were located near the drainage area, Site D at the pumping point, and Site E at the channel outlet. These locations allowed us to capture spatial variation in depth, hydrological setting, and exposure to external inputs, including sediment inflow during the period of channel construction.

2.2 Weekly stationary and biweekly vertical profile monitoring

From July 2022 to March 2024, water-quality monitoring was carried out at Sites A1, A0, B, C, D, and E using portable measuring instruments. Monitoring was conducted at Site A1 throughout this period, at Site A0 from October 2023 to March 2024, at Sites B and C from July 2022 to September 2023, and Sites D and E from September 2022 to September 2023 only when water was present in the channel (Fig. 1c). A0, A1, B, C, and D, measurements were conducted at two depths, 5 cm below the water surface and at the bottom, and vertical profiles were taken at 5 cm intervals from the water surface downward. These two types of measurements were conducted alternately on a biweekly basis between 10:00 and 15:00. At Sites D and E, only weekly stationary monitoring was conducted.

The measured parameters were pH, DO, Eh, electrical conductivity (EC), water temperature, and water depth. pH was measured using the PRN-41 (Fujiwara Scientific Co. LTD, Japan), and water depth was measured using a measuring stick. The other parameters were measured using the LAQUA-WQ310 (Horiba Scientific, Japan). The DO optode was model 300-D-2, the ORP electrode was model 9300-10D (reference electrode: 3.33 mol L^{-1} KCl-Ag/AgCl, metallic electrode: Pt), and the EC electrode was model 300-C-2 (sensor head) equipped with a 300-4C-C cartridge.

ORP values were converted to standard hydrogen electrode-based values (V vs. SHE), corrected for temperature, using the following equation:

$$E_{SHE} = (E_{Ag/AgCl} + 206 - 0.7(T - 25)) \quad (3)$$

2.3 High-resolution continuous monitoring

From October 17, 2023, to January, 15, 2024, continuous measurements of illuminance, temperature, DO, and Eh were conducted at 15-minute intervals. For Eh measurements, a fluorine-doped tin oxide (FTO) glass electrode was used as an alternative to a metallic electrode such as Pt, while a 3.33 mol L^{-1} KCl-Ag/AgCl electrode served as the reference electrode. Data were recorded using a voltage logger (LR5041, HIOKI E.E. Corp., Japan). To stabilize the FTO electrode, it was covered with approximately 1 cm of sediment on the sediment surface. Illuminance and temperature were measured using UA-002-64 sensors (Onset Computer Corp., USA), which were fixed 5 cm above the sediment surface and 10 cm below the water surface at Sites A0 and A1. Due to the difficulty of positioning the optical DO sensor (U26-001, Onset Computer Corp., USA) directly above sediment rich in fallen leaves, it was fixed 10 cm below the water surface at Site A1 instead.

2.4 Principal Component Analysis

Principal Component Analysis (PCA) was performed on the time-series data of pH, DO, Eh, EC, and temperature obtained from weekly stationary monitoring at Sites A0, A1, B, C, D, and E. The data periods analyzed were as follows: Site A1 from August 2, 2022, to January 17, 2024; Site A0 from September 22, 2022, to January 17, 2024; Sites B and C from August 2, 2022, to September 28, 2023; and Sites D and E from September 6, 2022, to August 21, 2023. Each dataset was normalized to have a mean of 0 and a variant of 1 before performing PCA. The PrincipalComponents function in Mathematica 12 was used for the analysis.

2.5 Discrete Fourier transformation (DFT)

We performed a DFT analysis on the six items of high-frequency monitoring variables to detect periodicities, using Mathematica 12's Fourier function. Additionally, we included hourly precipitation and average wind speed data provided by the Japan Meteorological Agency (JMA) at the location nearest to the pond (34°40.4′N, 135°50.2′ E, Nara) (JMA, 2023).

Before conducting the DFT, we carried out several preprocessing steps to enhance the detection of periodic components. First, a moving average was used to remove a clear downward trend, especially distinct in temperature data. The window size for the moving average was determined by calculating dataset's autocorrelation function (ACF), fitting a linear regression model to the ACF values to remove any baseline drift, and then detecting the strongest peak in the detrended ACF. The lag corresponding to the peak was chosen as the moving-average window size. To reduce spectral leakage in the DFT, a Hanning window was then applied to the data, preventing spurious high-frequency components. Finally, Mathematica 12's GaussianFilter function, with five neighboring samples on each side, was used to smooth out noise before running the Fourier function to detect periodicities.

2.6 Granger causality analysis with EcohNet

We applied EcohNet, a neural-network implementation of Granger causality (Suzuki et al. 2022), to 15-min records of surface and bottom temperature and luminosity, surface DO, and sediment-surface Eh. EcohNet selects the optimal set of causal variables X for a target variable Y to maximize predictive skill $\rho_{X \to Y}$. To test scale dependence, we also analyzed time-series data that were resampled to 30-min, 1-h, 6-h, 12-h, and 24-h intervals. For each of these coarser resolutions we repeated the analysis after phase-

shifting the sampling start time, thereby assessing the sensitivity of variable selection and predictive skill to sampling alignment. Because luminosity is determined exogenously by incoming solar radiation, it was excluded from the list of potential target variables.

3. Results

3.1 Site description

Across all monitoring sites in the pond (A0, A1, B, and C), water-column structure exhibited clear seasonal variations and vertical patterns during the 18-month survey (Fig. 2; Figs. S1−S2). Surface temperature ranged from 2.4 to 30.7ºC (mean 13.9ºC) and pH from 5.79 to 7.35 (mean 6.60). Strong leaf-litter inputs in autumn and low light levels at the sediment surface (≈0 lux) corresponded with persistent bottom-water anoxia throughout much of the year. Vertical DO profiles frequently showed near-surface oxygen depletion, consistent with high organic-matter loading and limited photosynthetic production.

The strongest physical disturbance occurred at Site A1 following channel construction. Sediment inflow that began in July 2023 sharply increased EC across the pond, most prominently at A1, and was accompanied by a 0.6-unit drop in bottom pH (Fig. 2). EC is widely used as an indicator of anthropogenic or sediment-mobilizing disturbances (Shrestha and Lal 2011; Yu et al. 2012), because fresh mineral exposure enhances ion release through accelerated weathering. This EC rise therefore provides an independent geochemical signature of the disturbance that also reshaped O_2 and Eh dynamics.

Following the opening of the inflow channel in August 2022, surface DO at A1 temporarily increased relative to A0, likely due to enhanced air-water mixing during

inflow events. In contrast, Site E, the channel outlet, experienced stagnation, and its DO during summer 2023 fell below levels recorded the previous year. From January to April 2024, DO at both A1 and A0 exceeded the values measured one year earlier, and Eh at A1 increased more strongly than at A0 (Fig. 2a), consistent with the spatial pattern of inflow-driven disturbance.

Principal component analysis based on five water-quality variables showed strong overlap among sites in the PC1-PC2 and PC1-PC3 spaces (Fig. 2b), indicating broadly similar water chemistry across the system. Seasonal variability dominated over spatial gradients, except for a notable displacement in PC1-PC2 space immediately after the July-August 2023 sediment inflow, further supporting the characterization of this event as a major disturbance.

3.2 ln[O_2]-Eh relationship from weekly monitoring and biweekly vertical profiles

The activity of O_2 was approximated by its molar concentration for all analyses. Across all sites and sampling dates with DO > 0 mg L^{-1}, Eh increased with ln[O_2] (pooled regression: Eh = 0.079 ln[O_2] + 1.15, adjusted R^2 = 0.382; Fig. 3a). Site-specific slopes were tightly grouped (0.075 to 0.093), and R^2 values ranged from 0.181 to 0.596 (Table S4). These results show that despite large seasonal variation in temperature and O_2 availability, the system maintained a consistent Nernstian slope, indicating a stable redox structure across most sites. Site D, which continuously received pumped water from the channel, showed the weakest ln[O_2]-Eh relationship (lowest R^2), suggesting that hydraulic forcing disrupted the prevailing redox structure.

Using the pooled slope and the observed temperature range (2.4−30.7ºC), the implied effective electron-transfer number was $n_{eff} \approx 0.30-0.33$. This value does not imply

240 that a fractional electron transfer at the level of individual reactions; rather, it reflects the
241 integrated electron flux from many simultaneous redox reactions that ultimately supply
242 electrons to O_2 (Fig. 1a).

243 To evaluate departures from this system-level relationship, we examined the
244 residuals between measured Eh and the Eh predicted from the pooled regression (cEh).
245 A pronounced shift occurred around June 15, 2023, coinciding with the resumption of
246 pumping at Site C and the onset of sediment inflow toward Site A1. At Site A1, residuals
247 increased sharply and remained elevated, indicating that the redox balance no longer
248 followed the established $\ln[O_2]$–Eh structure (Fig. 3b). Significant increases in $|cEh - Eh|$
249 in the three months before and after June 15 were detected at Sites A1 and B (Mann–
250 Whitney tests $p = 0.01$ and 0.02, respectively), confirming that the inflow event induced
251 a measurable collapse of the pre-existing redox regime.

252 Importantly, a follow-up vertical-profile survey in February 2025 revealed that
253 the original slope at Site A1 had re-emerged (blue points in Fig. 3a), demonstrating that
254 the system regained its prior redox structure after the disturbance.

255

256 **3.3 Short-term DO spikes do not perturb the prevailing redox structure**

257 Although weekly measurements suggested a robust, system-level relationship
258 between $\ln[O_2]$ and Eh, high-frequency logging at Site A1 showed that this stability does
259 not extend to sub-daily scales. During the October and December 2023 monitoring,
260 surface-water DO exhibited sharp increases (> 2 mg L^{-1}) whenever hourly rainfall
261 exceeded 5 mm (Fig. 4b). These rainfall-driven DO surges are consistent with enhanced
262 air-water gas exchange caused by surface turbulence (Jiang et al. 2018).

263 Despite these pronounced DO fluctuations, sediment-surface Eh remained

largely unchanged, and the ln[O_2]–Eh correlation collapsed during these events (R^2 < 0.01). This short-term decoupling indicates that bottom redox conditions are buffered against rapid hydrological disturbances, even when surface DO varies by an order of magnitude. Because such short-timescale perturbations are unlikely to reorganize the underlying redox structure, this asynchrony strengthens the interpretation that the ln[O_2]–Eh slope reflects a robust structural property of the redox network, not the instantaneous availability of O_2. Consistent with this interpretation, short-lived DO fluctuations do not reorganize the upstream reaction network that ultimately supplies electrons to O_2, whereas sustained disturbances such as the sediment inflow can.

3.4 Diurnal cycles and the absence of a detectable O_2 → Eh causal link

High-frequency measurements at Site A1 revealed a pronounced 24-h periodicity in bottom Eh, bottom temperature, and light availability (Fig. 4c), indicating that sediment-surface Eh responds primarily to diurnal forcing rather than to the episodic disturbances that dominate surface dynamics. In contrast, surface DO and surface temperature exhibited multi-day variability that closely followed rainfall and wind events, consistent with rapid meteorological control of surface-water conditions.

Phase decomposition of the 24-h components showed that bottom Eh lagged behind both bottom temperature and the onset of daylight by several hours (Fig. 5; Supplementary Discussion S2). This delayed response is consistent with Eh integrating a suite of temperature-dependent microbial and chemical processes, rather than responding instantaneously to changes in oxidant availability.

EchoNet causal analysis across multiple temporal resolutions (1-h, 30-min, 6-h, 12-h, and 24-h) consistently identified bottom temperature, and to a lesser degree surface

288 temperature, as causal predictors of bottom Eh, whereas surface DO never appeared in
289 the optimal predictor set (Fig. S4). This absence of a detectable $O_2 \rightarrow$ Eh causal link does
290 not imply that O_2 is irrelevant. Instead, it reflects the fact that O_2 influences Eh through
291 many intertwined reaction pathways whose effects are already embedded within Eh's own
292 time series, making the signal statistically inseparable. When a driver's influence is
293 dispersed across a highly interconnected reaction network, its unique contribution can fall
294 below the threshold of Granger-based detection, even when it plays a central chemical
295 role.

296 Together, these findings reinforce a key interpretation of the ln[O_2]–Eh
297 relationship. The robustness of the Nernstian slope arises not from instantaneous or causal
298 forcing by O_2, but from the stability of the upstream redox network that ultimately
299 supplies electrons to O_2. Temperature-driven changes modulate reaction rates within this
300 network, yet they do not reorganize its structure.

301

302 ## 4. Discussion

303 ### 4.1 Interpretation of n_{eff} as a system-level property

304 The Nernstian slope between Eh and ln[O_2] can be expressed in terms of an
305 effective electron-transfer number, n_{eff}. This quantity is sometimes misinterpreted as
306 providing information about the identity of electron donors. Our results illustrate why
307 such inference is not possible. If a single, well-defined reaction controlled O_2 reduction,
308 such as complete oxidation of organic matter or Fe^{2+} oxidation, then the number of
309 electrons transferred per mole of O_2 would be uniquely determined (e.g., $\geq$1 e^- mol^{-1} O_2
310 for most organic substrates). Under such conditions, n_{eff} would directly reflect that
311 reaction. However, in natural surface waters the electrons that ultimately reach O_2

originate from many partially coupled, parallel, and multi-step reactions (Fig. 1a). Complete or incomplete microbial oxidation of complex organic matter, nitrification steps, and iron redox cycling all contribute fluxes that differ in stoichiometry, reversibility, and timescale. When these fluxes are integrated by the electrode, the result is a mixed potential, and the inferred n_{eff} becomes a system-level aggregate, not a pathway-specific stoichiometric value.

Thus, the observed $n_{eff} \approx 0.3$ does not imply fractional electron transfer, nor does it allow identification of the dominant electron donor. Instead, it reflects the balance among multiple redox processes occurring simultaneously. The diagnostic value of n_{eff} lies in tracking changes in the structure of the redox network, not in determining which reduced species supplied electrons to O_2.

4.2 Why O_2 → Eh causality is not detected

Our causal analysis showed no significant statistical link from dissolved oxygen to bottom Eh, despite oxygen's central role as the terminal electron acceptor. This absence does not indicate chemical irrelevance of O_2; rather, it reflects the structure of the redox network. Because O_2 influences Eh through many parallel and coupled pathways, its effects become embedded within Eh's own time series and cannot be separated as a unique driver (Sugihara et al. 2012). In this sense, the robustness of the ln[O_2]–Eh slope arises not from direct, instantaneous or causal forcing by O_2, but from the stability of the upstream reaction network that mediates electron transfer to O_2.

4.3 Relationship between DO and Eh reported in previous studies

Previous studies have reported simultaneous measurements of Eh and DO

across a variety of environments, including wells, groundwater systems, and rivers. However, these datasets typically represent snapshots collected across multiple sites rather than long-term, co-located time series at a single location. After converting all reported Eh values to the standard hydrogen electrode scale and applying temperature corrections where possible, the aggregate relationship across ten published datasets showed a weak $\ln[O_2]$–Eh correlation ($R^2 = 0.18$; Fig. S5).

This weak cross-site correlation is consistent with expectations: spatially heterogeneous systems differ in organic-matter composition, dominant electron donors, hydrological regimes, and mineralogy, all of which influence Eh independently of O_2. As such, spatial comparisons inherently confound redox structure with environmental background conditions and are unlikely to yield a universal Eh–O_2 slope.

By contrast, our study uniquely examines long-term, co-located Eh and DO measurements within a single, seasonally forced system. Under these conditions, where the upstream reaction network evolves internally rather than being replaced by different external settings, the $\ln[O_2]$–Eh slope becomes much clearer and more stable. The stability of the slope across depths and seasons, and its collapse only under a discrete sediment-inflow disturbance, highlight that the relationship is meaningful primarily within a fixed redox-structural context, not across heterogeneous locations. Long-term, co-located monitoring is therefore essential for determining whether the $\ln[O_2]$–Eh relationship can serve as a reliable, site-specific indicator of redox structural stability.

4.4 Practical implications for monitoring shallow-water redox dynamics

Dissolved oxygen is among the most widely monitored variables in aquatic systems, partly because DO sensors are inexpensive, stable, and directly linked to key ecological

processes such as organic-matter degradation and community structure (Bastviken et al. 2004; Connolly et al. 2004; Wang et al. 2008; Franklin 2014). In contrast, Eh has been used far more selectively, despite the growing availability of robust, low-maintenance electrodes capable of continuous deployment (Vorenhout et al. 2004; Wang et al. 2022).

Our results demonstrate that neither DO nor Eh alone captures system-level redox dynamics, but their combination does. Long-term, co-located measurements provide a simple diagnostic for structural shifts in the redox network: the $\ln[O_2]$–Eh slope remains stable as long as the upstream electron-transfer pathways persist, and collapses only when the redox structure reorganizes. This emergent diagnostic requires no specialized instrumentation beyond sensors that are already in routine use.

Co-monitoring Eh and DO therefore represents a practical, low-cost approach for tracking qualitative changes in redox-system stability in ponds, wetlands, and other shallow-water environments. As inexpensive electrodes become more widely available, the Eh–O_2 relationship could become a valuable complement to existing DO-based ecological assessments.

5. **Conclusion**

This study demonstrates that the linear relationship between $\ln[O_2]$ and Eh provides a system-level indicator of redox structural stability in shallow aquatic environments. By integrating 18 months of depth-resolved profiles with high-frequency measurements in a disturbance-prone pond, we obtained three key insights.

(i) Persistence of a Nernstian slope across seasons

Across depths and seasons, Eh showed a consistent Nernstian dependence on $\ln[O_2]$,

indicating that the upstream redox network maintained a stable pseudo–steady state despite large environmental fluctuations. The tight grouping of site-specific slopes (0.075–0.093 V) suggests that this structural stability is a characteristic emergent property of the system.

(ii) Sensitivity to structural disturbance

A discrete sediment-inflow event temporarily collapsed the $\ln[O_2]$–Eh slope at the impacted site, and residual analyses confirmed a measurable breakdown of the prevailing redox structure. Recovery of the original slope several months later further supports the interpretation that deviations from the $\ln[O_2]$–Eh relationship provide an effective signature of redox reorganization.

(iii) Embedding of oxygen influence embedded within the network.

High-frequency observations and causal-network analysis revealed that DO does not act as an isolated predictor of Eh. Instead, oxygen's influence is dispersed across many intertwined pathways, rendering its direct causal footprint statistically inseparable. Temperature emerged as the dominant predictor, reflecting its modulation of reaction rates within the redox network rather than its control over structural configuration.

These findings show that the $\ln[O_2]$–Eh slope is not a snapshot of oxidant availability, but a dynamic fingerprint of the underlying electron-transfer network. Continuous, co-located monitoring of Eh and DO offers a simple, low-cost, and broadly applicable method for identifying qualitative shifts in redox-system structure, information that cannot be inferred from either variable alone. As automated Eh sensors become more

accessible, this combined approach holds strong potential for tracking redox stability in ponds, wetlands, and other shallow-water ecosystems.

Acknowledgments:

This study was supported by JSPS KAKENHI Grant Numbers 24K01844 to MS, MI, and KI, and the Iwatani Naoji Foundation and 24H01514 to MS. The authors are grateful to the comments from Ryuhei Nakamura, Hideshi Ooka, and Hiroyuki Kashima.

Author Contribution

M.S. conceived the theoretical framework and designed the study.

M.I. and K.I. designed the experimental setup and installed the logging devices.

K.M. conducted the monitoring, curated the datasets, and performed the initial formal analyses.

M.S. led the analysis design, interpreted the results, and wrote the manuscript with input from all authors.

References

Bastviken, D., L. Persson, G. Odham, and L. Tranvik. 2004. Degradation of dissolved organic matter in oxic and anoxic lake water. Limnology & Oceanography **49**: 109–116. doi:10.4319/lo.2004.49.1.0109

Borch, T., R. Kretzschmar, A. Kappler, P. V. Cappellen, M. Ginder-Vogel, A. Voegelin, and K. Campbell. 2010. Biogeochemical redox processes and their impact on

contaminant dynamics. Environ. Sci. Technol. **44**: 15–23. doi:10.1021/es9026248

Connolly, N. M., M. R. Crossland, and R. G. Pearson. 2004. Effect of low dissolved oxygen on survival, emergence, and drift of tropical stream macroinvertebrates. Journal of the North American Benthological Society **23**: 251–270. doi:10.1899/0887-3593(2004)023%3C0251:EOLDOO%3E2.0.CO;2

Franklin, P. 2014. Dissolved oxygen criteria for freshwater fish in New Zealand: a revised approach. New Zealand Journal of Marine and Freshwater Research **48**: 112–126. doi:10.1080/00288330.2013.827123

Jiang, Z., X. Li, W. Jin, X. Yu, and Z. Zhou. 2018. Planar optode observation method for the effect of raindrop on dissolved oxygen and pH diffusion of air–water interface. Exp Fluids **59**: 175. doi:10.1007/s00348-018-2631-z

Lau, M. P., R. Niederdorfer, A. Sepulveda-Jauregui, and M. Hupfer. 2018. Synthesizing redox biogeochemistry at aquatic interfaces. Limnologica **68**: 59–70. doi:10.1016/j.limno.2017.08.001

Lindberg, R. D., and D. D. Runnells. 1984. Ground water redox reactions: an analysis of equilibrium state applied to eh measurements and geochemical modeling. Science **225**: 925–927. doi:10.1126/science.225.4665.925

Ramesh Kumar, A., and P. Riyazuddin. 2012. Seasonal variation of redox species and

redox potentials in shallow groundwater: A comparison of measured and calculated redox potentials. Journal of Hydrology **444–445**: 187–198. doi:10.1016/j.jhydrol.2012.04.018

Shrestha, R. K., and R. Lal. 2011. Changes in physical and chemical properties of soil after surface mining and reclamation. Geoderma **161**: 168–176. doi:10.1016/j.geoderma.2010.12.015

Stefánsson, A., S. Arnórsson, and Á. E. Sveinbjörnsdóttir. 2005. Redox reactions and potentials in natural waters at disequilibrium. Chemical Geology **221**: 289–311. doi:10.1016/j.chemgeo.2005.06.003

Stumm, W., and J. J. Morgan. 1996. Aquatic chemistry: Chemical equilibria and rates in natural waters, 3rd ed. J. Wiley & sons.

Sugihara, G., R. May, H. Ye, C. Hsieh, E. Deyle, M. Fogarty, and S. Munch. 2012. Detecting causality in complex ecosystems. Science **338**: 496–500. doi:10.1126/science.1227079

Suzuki, K., S. S. Matsuzaki, and H. Masuya. 2022. Decomposing predictability to identify dominant causal drivers in complex ecosystems. Proc. Natl. Acad. Sci. U.S.A. **119**: e2204405119. doi:10.1073/pnas.2204405119

Tandon, P. K., and S. B. Singh. 2016. Redox processes in water remediation. Environ

Chem Lett **14**: 15–25. doi:10.1007/s10311-015-0540-4

Teasdale, P. R., A. I. Minett, K. Dixon, T. W. Lewis, and G. E. Batley. 1998. Practical improvements for redox potential (EH) measurements and the application of a multiple-electrode redox probe (MERP) for characterising sediment in situ. Analytica Chimica Acta **367**: 201–213. doi:10.1016/S0003-2670(98)00171-8

Violante, A., V. Cozzolino, L. Perelomov, A. G. Caporale, and M. Pigna. 2010. Mobility and bioavailability of heavy metals and metalloids in soil environments. J. Soil Sci. Plant Nutr. **10**. doi:10.4067/S0718-95162010000100005

Vorenhout, M., H. G. Van Der Geest, D. Van Marum, K. Wattel, and H. J. P. Eijsackers. 2004. Automated and continuous redox potential measurements in soil. J of Env Quality **33**: 1562–1567. doi:10.2134/jeq2004.1562

Wang, S., X. Jin, Q. Bu, L. Jiao, and F. Wu. 2008. Effects of dissolved oxygen supply level on phosphorus release from lake sediments. Colloids and Surfaces A: Physicochemical and Engineering Aspects **316**: 245–252. doi:10.1016/j.colsurfa.2007.09.007

Wang, X., Y. Wu, N. Chen, H. Piao, D. Sun, H. Ratnaweera, Z. Maletskyi, and X. Bi. 2022. Characterization of oxidation-reduction potential variations in biological wastewater treatment processes: a study from mechanism to application.

Processes **10**: 2607. doi:10.3390/pr10122607

Yu, S., G. B. Yu, Y. Liu, G. L. Li, S. Feng, S. C. Wu, and M. H. Wong. 2012. Urbanization impairs surface water quality: eutrophication and metal stress in the grand canal of china. River Research & Apps **28**: 1135–1148. doi:10.1002/rra.1501

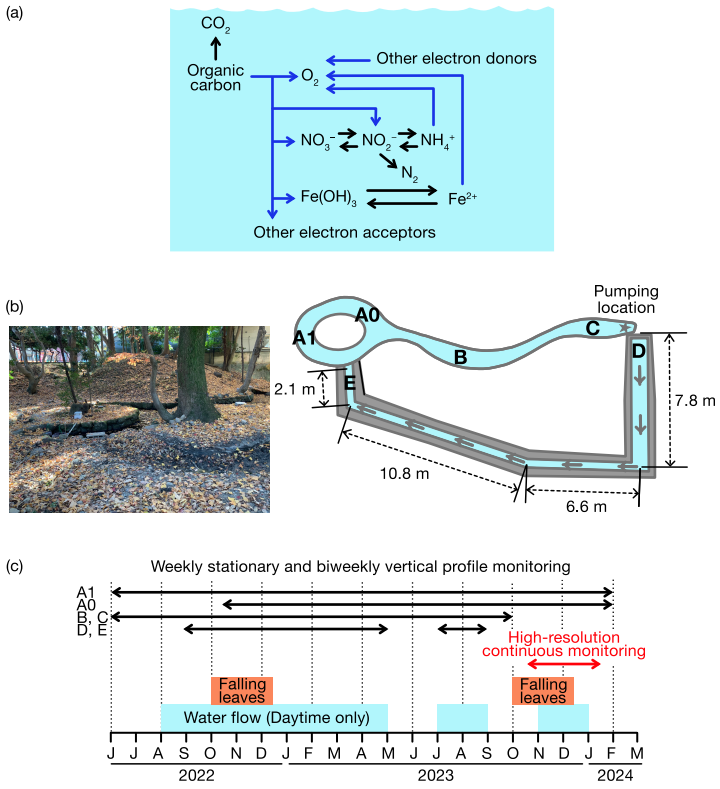

Figure 1: Conceptual diagram of electron flux in the upstream redox network (a), locations of monitoring sites (b), and major events during the monitoring period (c). (a) Schematic representation of the upstream redox network that supplies electrons to O_2, the terminal electron acceptor. Blue arrows denote electron flow and black arrows denote mass flow among representative pathways (organic-matter oxidation, nitrogen transformations, and iron cycling). (b) Map of the artificial pond and surrounding water channel showing all monitoring sites. (c) Timeline of key events: the water channel was opened in May 2022 and expanded in May 2023; daytime solar-powered pumping transferred water from the star-marked location in the pond to Site D, after which the water was discharged from Site E back into Site A1.

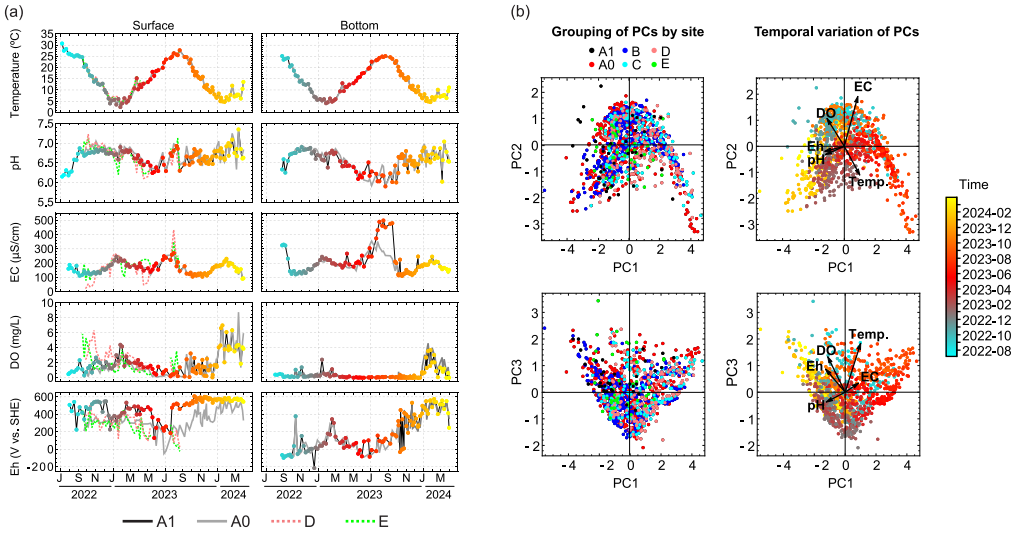

Figure 2: (a) Seasonal trends of temperature, pH, EC, DO, and Eh at Sites A1, A0, D, and E. (b) Principal component analysis (PCA) of five water-quality parameters (pH, DO, Eh, EC, and temperature) based on weekly monitoring. The upper and lower rows show PC1-PC2 and PC1-PC3 relationships, respectively. The left column displays site-level grouping, and the right column shows temporal variation with loading vectors. Colored points represent monitoring dates. Loading vectors are scaled by a constant factor for clarity.

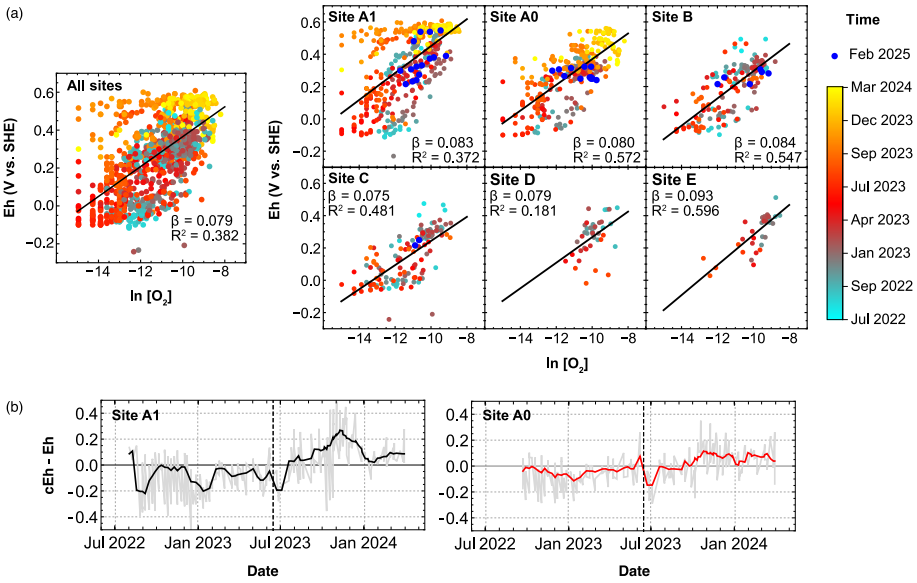

Figure 3: Relationship between ln[O_2] and Eh, and residuals between predicted and observed Eh. (a) ln[O_2]-Eh relationships from weekly stationary and biweekly vertical-profile monitoring, shown for all sites (left) and individually for Sites A1, A0, B, C, D, and E. Solid lines indicate site-specific regression fits, with β denoting the slope. Point colors represent monitoring dates. (b) Residuals (cEh - Eh) at Sites A1 and A0, where cEh is the Eh predicted from the pooled regression. The dashed vertical line marks June 15, 2023, when water pumping from Site C and drainage to Site A1 resumed.

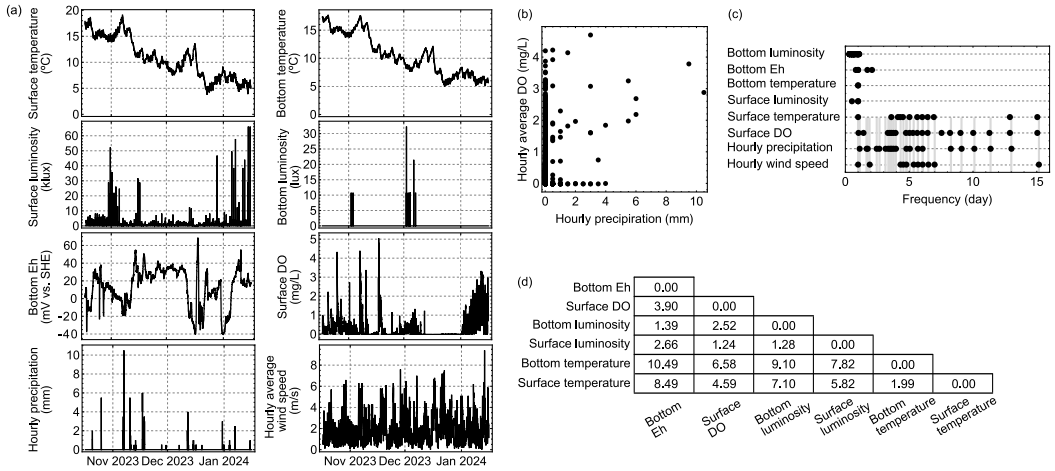

Figure 4: Relationship between high-frequency monitoring data (15-min intervals) and hourly meteorological drivers. (a) Time-series records of surface and bottom temperature, luminosity, sediment-surface Eh, surface DO, and hourly precipitation and wind speed from October 2023 to January 2024. (b) Relationship between hourly precipitation and the hourly mean DO concentration. (c) Periods of major spectral components identified by discrete Fourier transform (DFT) analysis. Major components were defined as those with amplitudes $\geq 50\%$ of the maximum amplitude. Gray vertical lines show the dominant periodicities of precipitation and wind speed. (d) Absolute phase differences among the 1-day components extracted from DFT analysis. Eh measurements used a fluorine-doped tin oxide (FTO) working electrode and a 3.33 mol L^{-1} KCl-Ag/AgCl reference electrode.

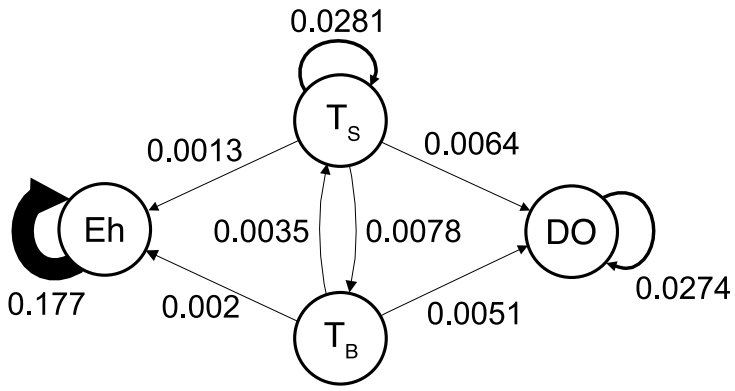

Figure 5: Causal network inferred from high-frequency time-series data (October 17, 2023-January 15, 2024), down-sampled to a 1-hour interval. Nodes represent Eh, surface temperature (T_S), bottom temperature (T_B), and surface DO; arrows denote significant causal links identified by EcohNet, with numbers indicating predictive skill ($\rho_{X\to Y}$). Self-loops represent the contribution of each variable ' s own past state. Eh was measured using a fluorine-doped tin oxide (FTO) glass working electrode with a 3.33 mol L^{-1} KCl-Ag/AgCl reference electrode.